ACS APPLIED MATERIALS & INTERFACES

Research Article

Cite This: ACS Appl. Mater. Interfaces 2019, 11, 13777−13786

www.acsami.org

Fluorescence-Based Observation of Transient Electrochemical and Electrokinetic Effects at Nanoconfined Bipolar Electrodes

Karen Scida,[†] Alexander Eden,[†] Netzahualcóyotl Arroyo-Currás,[‡] Sean MacKenzie,[†] Yesil Satik,[†] Carl D. Meinhart,[†] Jan C. T. Eijkel,[§] and Sumita Pennathur*[,†]

[†]Department of Mechanical Engineering, University of California Santa Barbara, Santa Barbara, California 93106, United States

[‡]Department of Pharmacology and Molecular Sciences, Johns Hopkins University School of Medicine, Baltimore, Maryland 21205, United States

[§]Department of Electrical Engineering, Mathematics and Computer Science, University of Twente, Enschede, Overijssel 7522, The Netherlands

Supporting Information

ABSTRACT: Bipolar electrodes (BPEs) are conductors that, when exposed to an electric field, polarize and promote the accumulation of counterionic charge near their poles. The rich physics of electrokinetic behavior near BPEs has not yet been rigorously studied, with our current understanding of such bipolar effects being restricted to steady-state conditions (under constant applied fields). Here, we reveal the dynamic electrokinetic and electrochemical phenomena that occur near nanoconfined BPEs throughout all stages of a reaction. Specifically, we demonstrate, both experimentally and through numerical modeling, that the removal of an electric field produces solution-phase charge imbalances in the vicinity of the BPE poles. These imbalances induce intense and short-lived nonequilibrium electric fields that drive the rapid transport of ions toward specific BPE locations. To determine the origin of these electrokinetic effects, we monitored the movement and fluorescent behavior (enhancement or quenching) of charged fluorophores within well-defined nanofluidic architectures via real-time optical detection. By systematically varying the nature of the fluorophore, the concentration of the electrolyte, the strength of the applied field, and oxide growth on the BPE surface, we dissect the ion transport events that occur in the aftermath of field-induced polarization. The results contained in this work provide new insights into transient bipolar electrokinetics that improve our understanding of current analytical platforms and can drive the development of new micro- and nanoelectrochemical systems.

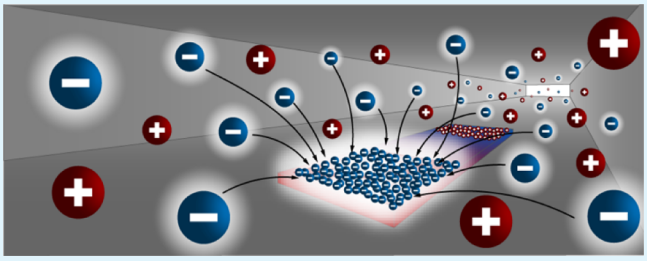

KEYWORDS: *bipolar electrode, electrokinetics, electrochemistry, water electrolysis, nanoconfinement, fluorescence, electric double layer*

INTRODUCTION

The thorough understanding of electrokinetic phenomena is important not just fundamentally but for the development of innovative techniques, such as electrodiffusiophoresis[1] and contact charge electrophoresis,[2] that can support key analytical applications across synthetic chemistry (e.g., enantiomeric separations[3]), clinical practice (e.g., real-time sorting of healthy vs cancerous cells in blood[4]), and environmental remediation.[5] One such electrokinetic phenomenon—the bipolar effect[6]—manifests when an electric field exists at the interface between an electroconductive material and an electrolyte solution. The field induces electric polarization of the conductor, leading to a rearrangement of the surface charge distribution that results in accumulation of positive and negative charges at two opposite poles of the material, thus coining the term bipolar electrodes or BPEs. Furthermore, the redistribution of surface charges produces electric double layers (EDLs) in the electrolyte solution surrounding the poles. Such electric field-induced polarization of BPEs has already been used for numerous applications, including to strategically focus (de-mix) heterogeneous solutions[7] or stir electrolyte solutions.[8]

The properties of BPEs in solution can also be modulated to promote coupled redox reactions at BPE poles, a technique called bipolar electrochemistry.[6,9−11] Under appropriate conditions, bipolar electrochemical systems will not only cause ion motion and separation but will also produce faradaic reactions that generate additional electron−ion interactions and modify the subsequent behavior of the system. For example, the oxidation of water in acidic media ($2H_2O = 4e^- + O_2 + 4H^+$) generates ions from neutral species, while proton reduction reaction in acidic solutions ($2H^+ + 2e^- = H_2$) neutralizes charged species. Many other reactions increase or decrease the total ionic charge content, such as the iron reduction reaction ($Fe^{3+} + e^- = Fe^{2+}$). These phenomena have

Received: January 21, 2019
Accepted: March 18, 2019
Published: March 18, 2019

DOI: 10.1021/acsami.9b01339
ACS Appl. Mater. Interfaces 2019, 11, 13777−13786

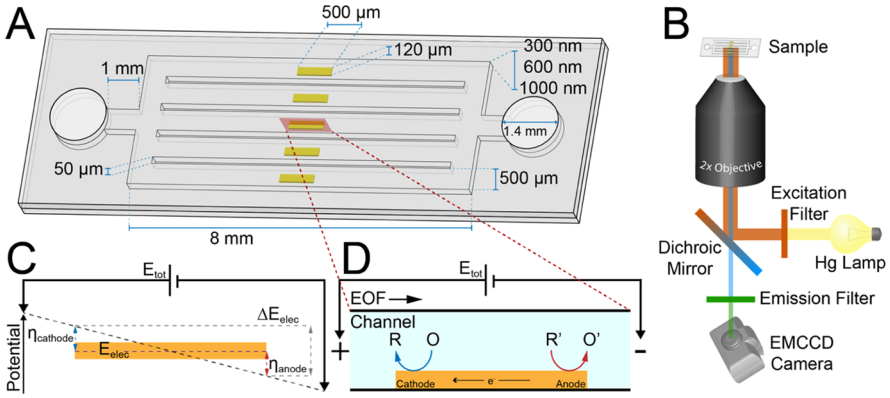

Figure 1. Experimental approach and principles of bipolar electrochemistry. (A) We fabricated of glass-on-glass devices containing five nanochannels each with embedded BPEs (yellow) and used an (B) epifluorescence setup to monitor transient electrochemical and electrokinetic effects near nanoconfined BPEs. (C,D) When a conductor (i.e., the BPE) is immersed within an ionic solution and exposed to an electric field, it polarizes. If the polarization is large enough to induce (C) sufficient overpotentials at each pole ($\eta_{cathode}$ and η_{anode}), then (D) simultaneous oxidation and reduction reactions occur at opposing poles. We systematically reveal the unique electrokinetic, electrochemical, and fluorescent phenomena that occur upon removal of the electric field by varying electrolyte concentrations, pH, fluorophore, E_{tot}, and oxide growth on the BPE surface.

previously been exploited to create micro- and nanomotors based on unipolar water electrolysis,[12,13] screen electrocatalysts,[14−16] detect DNA,[17] and generate pressure-driven valves.[18] Of interest to electrokinetic systems, BPEs can induce concentration polarization by electrochemically generating ion depletion zones. For example, OH^- produced via water reduction can be used to strategically neutralize buffer cations, creating regions of low conductivity (and thus high electric fields) nearby the BPE cathode. Such fields can be exploited to preconcentrate charged fluorophores 500,000-fold in determined locations along a microchannel.[19] Using the same concept, a mixture of charged fluorophores—each with a different electrophoretic mobility (μ_{ep})—can be separated and preconcentrated within a single channel[20] or manipulated for permanent separation in different channels.[21]

Exploiting BPE physics in nanochannels offers key advantages over the aforementioned micro- and macroscale applications as confinement enhances liquid−surface interactions, increases the ability to manipulate small fluid volumes, and improves limits of detection. Indeed, electric field-induced movement of electrons, ions, and neutral molecules around nanoconfined BPEs has already proved useful. For example, Gao et al.[22] created a BPE/glass nanopore system which tracked ionic current passing through the pore overtime in the presence of an electric field. By monitoring the ongoing BPE reaction, which produced H_2 molecules and Ag^+ ions, the authors obtained limits of detection down to 14 molecules and 28 ions, respectively. Similarly, Wood and Zhang used both amperometric and optical monitoring to dynamically control the electrochemically driven bipolar growth of Au nanowires inside silica nanochannel templates.[23]

All studies to date, however, are limited to conditions of steady state, wherein the magnitude of an externally applied electric field remains constant throughout the experiment. Once this field is removed, electrons and ions will transition from perturbed states to equilibrium. Very little is known about the interplay between electrons and ions during this transition, though the implications of such knowledge could be of paramount importance to understanding diverse electrokinetic phenomena from proton-coupled electron transfer[24−26] in nanoconfinement, to the lifetime of solvated electrons,[27,28] to the rates of electron tunneling as a function of diffuse layer density and composition.[29,30] To shed light on these previously unexplored dynamics, we exploit the advantages of bipolar electrochemistry in nanoconfinement to reveal the electron−ion interactions that take place immediately after removal of an externally applied electric field.

RESULTS AND DISCUSSION

We employed a two-pronged approach to elucidate the complex events occurring near a nanoconfined BPE. In the experimental arm, we fabricated nanofluidic devices consisting of rectangular platinum BPEs confined to nanometer-sized channels (Figure 1A) and optically monitored the motion of ions in real time with electrolyte solutions containing fluorophores (Figure 1B). Specifically, we systematically varied electrolyte concentrations, pH, total applied potential (E_{tot}), and oxide growth on the BPE surface and measured fluorescence emission to infer the behavior of electrons and ions surrounding the BPE. A list of all conditions and species involved in each experiment is provided in Table S1 of the Supporting Information section. In parallel, we developed a finite element-based numerical model to qualitatively represent our experimental system. The numerical model accounts for ionic migration and diffusion, advection by electroosmotic and pressure-driven flows, EDLs, acid−base equilibria of the buffer, and the kinetics of all participating redox reactions (see the Supporting Information for details).

Principles of Bipolar Electrochemistry. The basic principles of bipolar electrochemistry and the behavior of bipolar electrochemical systems under conditions of the steady state or quasi-steady state (i.e., in the presence of a constant applied electric field) have been described extensively.[9,11,31,32] Briefly, a uniform electric field forms when a potential (E_{tot}) is applied across an electrolyte-filled nanochannel with insulated walls. If a conductor (i.e., the BPE) is placed within the solution-filled channel (Figure 1C), it floats to an equilibrium potential (E_{elec}) which is lower than the adjacent fluid potential at one end ($\eta_{cathode}$) and higher than the fluid potential at the other (η_{anode}). Under the right conditions, these interfacial potential differences—that is, the overpotentials ($\eta_{cathode}$ and η_{anode})—can drive distinct yet coupled electrochemical

DOI: 10.1021/acsami.9b01339
ACS Appl. Mater. Interfaces 2019, 11, 13777−13786

reactions on either pole of the BPE (Figure 1D). The magnitude of the combined overpotentials (ΔE_{elec}, Figure 1C) determines the probability of redox reactions occurring:[33] for significant reactions to proceed, ΔE_{elec} must be larger than the cell potential ($E^{o\prime}_{cell}$) of the reactions of interest. Importantly, ΔE_{elec} can be approximated as a function of the applied potential by

$$\Delta E_{elec} = E_{tot}\frac{l_{BPE}}{l_{channel}} \quad (1)$$

where l_{BPE} and $l_{channel}$ are the lengths of the BPE and channel, respectively. We use this equation as a guide to elucidate dynamic electrochemical processes at BPEs.

Qualitative Description of Experimentally Observed Phenomena. To visualize the electric field-induced BPE electrokinetic phenomena and electrochemical reactions in real time, we monitored the fluorescence intensity of the charged (−2 at pH > 6.4[34]), pH-sensitive[32,35] fluorophore fluorescein (FL) before, during, and after application of E_{tot} (Figure 2).

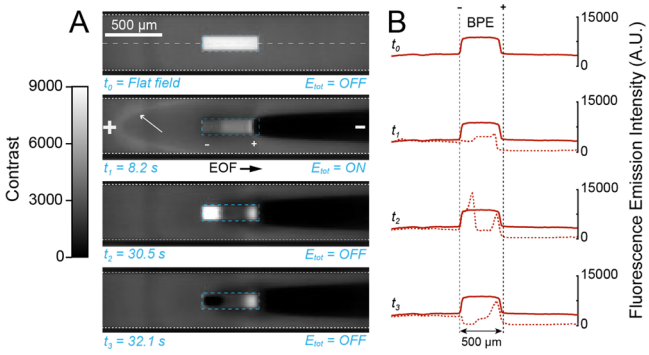

Figure 2. Real-time optical monitoring of nanoconfined bipolar electrochemistry. (A) Tracking of the fluorescence emission intensity of a solution containing 1.0 mM phosphate and 100 μM fluorescein at pH 7.5 before (t_0), during (t_1), and after (t_2 and t_3) the application of E_{tot} = 250 V in a 600 nm tall channel. (B) Fluorescent emission intensity profiles were quantified as a function of position along the length of the channel (indicated with yellow dashed line in A, t_0). For reference, we added the flat-field fluorescent intensity (solid red trace) on all profiles. Note that the flat-field fluorescence intensity at the BPE is double that elsewhere in the channel due to reflection from the metal surface. Application of the electric field induces polarization along the electrode and drives water electrolysis (t_1). Immediately after E_{tot} is removed (at t = 30 s), we observe enhancement of the fluorescence emission intensity at the left pole and recovery of flat-field fluorescence levels at the right pole (t_2), followed closely by rapid quenching at the left pole (t_3).

The resulting electric field induces electron redistribution along the surface of the BPE (polarization) and, because of electrostatic metal-ion interactions, drives the formation of charge-separated EDLs (on the order of 10 nm in size for 1.0 mM ionic solutions, Figure S1) in the immediate vicinity of the BPE poles. An EDL of positive charge density forms at the left BPE pole[a] (cathode) due to the accumulation of cations and repulsion of anions, resulting in localized decrease of fluorescence intensity (Figure 2, t_1). Conversely, an EDL of negative charge density forms at the right BPE pole (anode), generated by the accumulation of anions and repulsion of cations. In fact, we observed a small and localized increase in fluorescence intensity at the right pole, but this was accompanied by large regions of darkness in the vicinity. This fluorescence quenching (due to water electrolysis) will be explained in the next section.

Upon removal of the externally applied electric field (Figure 2, t_2), we observed localized fluorescence enhancement (above flat field levels, t_0) at the left pole. Simultaneously, the right pole showed recovery of fluorescence intensity back to flat field levels. These events are followed 1.6 s later by a complete quenching of fluorescence at the left pole (Figure 2, t_3). Only after these events have occurred does the system return to equilibrium conditions (Movie S1), with the overall fluorescence intensity returning to near-flat field levels (at the culmination of the test, ∼10% of the fluorescence signal is lost because of photobleaching, Figure S2). These observations, in the presence and after the removal of the externally applied electric field, can be explained by a number of coupled mechanisms, which we describe next, first with a qualitative numerical simulation, and then with systematic experiments to validate our model.

Dynamics while E_{tot} in ON. If the externally applied electric field is sufficiently large (i.e., $\Delta E_{elec} > E^{o\prime}_{cell}$), high rates of water electrolysis can be observed at the BPE poles, the equations for which are given by[36]

$$O_2 + 4H^+ + 4e^- \rightleftharpoons 2H_2O \text{(water oxidation at acidic pH)} \quad (2)$$

$$O_2 + 2H_2O + 4e^- \rightleftharpoons 4OH^- \text{(water oxidation at basic pH)} \quad (3)$$

$$2H^+ + 2e^- \rightleftharpoons H_2 \text{(water reduction at acidic pH)} \quad (4)$$

$$2H_2O + 2e^- \rightleftharpoons H_2 + 2OH^- \text{(water reduction at basic pH)} \quad (5)$$

These reactions will change the pH and conductivity of the electrolyte near the BPE poles. Specifically, the water oxidation reaction at the right pole generates O_2 and decreases the solution pH due to either generation of H^+ (eq 2) or consumption of OH^- (eq 3). Conversely, the water reduction reaction occurring at the left pole generates H_2 and increases the solution pH via consumption of H^+ (eq 4) or generation of OH^- (eq 5).

At the nanoscale, the reaction conditions will depend on the BPE length and nanochannel dimensions, as well as, of course, the applied potential (eq 1). This, together with previous reported knowledge of the physics involved,[9,11,31,32] allows us to predict the electrochemical and electrokinetic behavior of our system at the steady state. As the water oxidation reaction proceeds at the right pole, the combined effect of decreased pH[37,38] (Figure S3A) and O_2 generation[39,40] is expected to cause quenching of FL fluorescence intensity. Meanwhile, as the water reduction reaction proceeds at the left pole, the resulting pH increase should maintain FL fluorescence intensity near-flat field levels (Figure S3A). In a nanochannel, these reaction-dependent changes will be exacerbated[32] because of the small amount of overall ions initially present and the weak buffering capacity of the system (i.e., 1.0 mM phosphate).

Additionally, FL will also undergo a net charge change with changing pH: from $FL^{-1/-2}$ to FL^0 (at pH < 4) and from FL^0 to FL^+ (at pH < 2).[34,39,41] The electrostatic repulsion of cations (H^+ and FL^+) from the right pole and the downstream transport of FL^0 and proton-rich (or hydroxide-depleted) fluid by electro-osmotic flow (EOF) is expected to generate an overall decrease in fluorescence intensity at the right pole and a

DOI: 10.1021/acsami.9b01339
ACS Appl. Mater. Interfaces 2019, 11, 13777−13786

black "wake" to the right of the BPE (Figure 2, t_1). Meanwhile, even though the electrochemically induced pH increase at the left pole should maintain the fluorescence intensity of FL near flat field levels (Figure S3A), the electrostatic repulsion of anions (i.e., $FL^{-1/-2}$ and OH^-) is expected to decrease the overall fluorescence above that pole. Finally, because the migration of OH^- is opposite to the EOF and faster than $FL^{-1/-2}$ migration by virtue of its higher mobility, we expect to observe higher fluorescence intensity at the interface between the OH^- tail and the $FL^{-1/-2}$ front to the left of the BPE (indicted by the white arrow in Figure 2A, t_1, and observed also in Movie S1).

The steady-state predictions match our experimentally observed results in the presence of an applied electric field (Figure 2, t_0 vs t_1). However, our interest is in elucidating the dynamics after the removal of the external electric field.

Dynamics after E_{tot} is Removed. At the nanoscale, we can assume that the EDLs are an important factor in this system. The interesting dynamics observed at t_2 and t_3 in Figure 2 are the product of rich, coupled electrokinetic and electrochemical events driven by residual electric forces and ionic gradients in the nanochannel. To mechanistically understand how such temporary charge imbalances drive the observed dynamics in Figure 2, we analyzed transient numerical simulation results of longitudinal electric fields, BPE surface charge, and ion concentration profiles within the EDL regions above the BPE (Figure 3). It is important to note

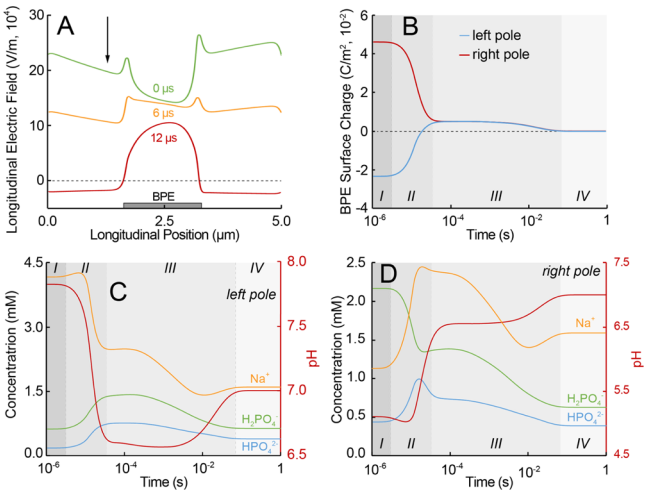

Figure 3. Finite element simulations of coupled electrokinetic–electrochemical dynamics along nanoconfined BPEs. We explored the rapid and spontaneous electrokinetic and electrochemical effects generated when a potential (E_{tot}) applied across a channel containing a BPE is turned OFF (parameters listed below). In the process of achieving equilibrium, (A) longitudinal electric field changes direction to balance out differences between the EDLs and the (B) BPE surface charge at the poles. Consequently, migration of ions is induced toward the (C) left and (D) right poles, affecting the local pH. Regions I through IV represent the four main stages of the system's relaxation process. Simulation parameters: Channel (5 μm long × 600 nm tall × 500 μm wide); BPE (1.67 μm long × 100 nm tall × 120 μm wide); E_{tot} = 1.4 V until steady state is reached and then ramped down from 2 to 12 μs; initial pH = 7; all concentration/pH profiles and electric field transients were obtained 10 nm directly above BPE pole edges (i.e., at the intersection between the white dotted lines, Figure S1). Note that all time scales are relative to the time elapsed after the removal of E_{tot}.

that due to computational restrictions, we could not exactly match the channel and BPE dimensions to those of the experiments. As a consequence, some time-dependent processes occurred at different time scales between experiments and simulation. However, we were able to match key time scales (i.e., transverse diffusion and migration, transverse Debye and Stern layer, longitudinal diffusion and migration differences, and electrochemical reaction rates, see Tables S2–S4) that allow us to qualitatively understand the origin and nature of the mechanisms involved in our experimental observations.

Our simulations predict that short-lived, nonequilibrium charge distributions in the EDLs and BPEs lead to a reversal of the electric field direction (0 vs 12 μs, Figure 3A). In accordance with Gauss's law, these electric fields attract counterionic charge to screen and ultimately neutralize the charge imbalances as the system progresses toward equilibrium. Specifically, a two-step relaxation occurs upon removal of E_{tot}. First, and immediately after removal of E_{tot}, accumulated ions at the poles (i.e., the EDLs) cause the BPE to remain at the same polarization as when E_{tot} was ON [Figure 3B–D(I)]. This polarization dissipates via drift-diffusion of ions (ohmic relaxation), with a half-life of ~13 μs [Figure 3B–D(II)] in our simulation. It is during this first relaxation step that we observe fluorescence enhancement at the left pole (Figure S4A), as anionic FL migrates to neutralize the positive space charge in the EDL (together with OH^-, PO_4^{3-}, HPO_4^{2-}, and $H_2PO_4^-$ and outflux of cations, such as Na^+). The largest influx is experienced by HPO_4^{2-} and $H_2PO_4^-$ buffer ions, causing temporary acidification of the electrolyte [Figure 3C(II)]. At the right pole, conversely, the negatively charged EDL is neutralized by a large influx of cations along with alkalization of the electrolyte, driven by a rapid exchange of HPO_4^{2-} and $H_2PO_4^-$ buffer species [Figure 3D(II)]. As the EDL relaxes, the BPE polarization dissipates; however, a net positive charge remains [akin to a charged Galvanic cell, Figure 3B(III)]. At this point, the unipolar BPE undergoes galvanic discharge via the oxidation of water (Figure S4B),[42] before finally reaching equilibrium and pH neutrality [Figure 3B–D(IV)]. It is this second relaxation event (i.e., BPE discharge), with a half-life of ~5–10 ms in the simulation, that produces the fluorescence quenching observed at the left pole. This latter prediction is experimentally validated in the next section.

Overall, our simulated results are in good agreement with our experimental observations which show initial enhancement of fluorescence intensity at the left pole (Figure 2, t_2) due to the influx of FL anions, followed by acidification-induced quenching (Figure 2, t_3) and a return to flat field levels due to pH neutralization (Movie S1).

Water Oxidation during BPE Discharge. According to our simulations, the sudden drop in fluorescence intensity at the left pole is caused by water oxidation-driven changes in pH and O_2 concentration when the BPE discharges. Here, we reveal three experiments performed to empirically demonstrate the validity of our model's prediction.

BPE discharge via the oxidation of water should cause FL quenching not only at the left pole but also everywhere on the BPE. However, our experimental results demonstrate that this is not the case. Such discrepancy could be accounted for by electrochemical modification of the BPE surface during application of the applied field. To prove this, first, we electrochemically deposited and removed Pt oxide by

DOI: 10.1021/acsami.9b01339
ACS Appl. Mater. Interfaces 2019, 11, 13777–13786

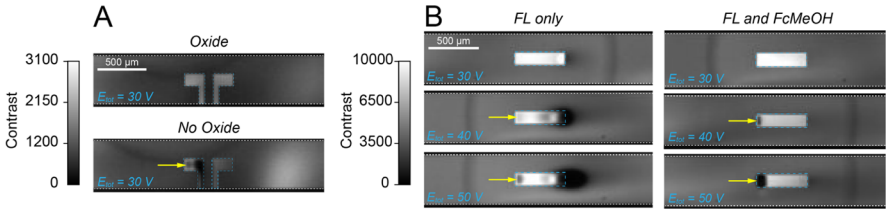

Figure 4. Quenching at the left pole is linked to water oxidation products. (A) By filling a 500 nm tall channel with a mixture of 1.0 mM phosphate (pH 8) and 100 μM FL containing a split BPE, we demonstrate that fluorescence quenching occurs only at the left pole due to the growth of Pt oxides at the right pole when E_{tot} is ON. Note that both images were acquired at the same experimental time. (B) By scanning E_{tot} from 20 V (not shown) to 50 V in a 1000 nm tall channel containing 1.0 mM phosphate (pH 8 and 1.3 mS/cm^2) and 100 μM FL or 100 μM FL and 5 mM FcMeOH, we confirmed that the decrease in fluorescence emission intensity at the left pole upon removal of E_{tot} is caused by the products of water oxidation driving pH- and/or O_2-induced quenching.

oxidation and reduction, respectively, on a split BPE[43,44] before performing fluorescence experiments. In this setup (Figure 4A), we used the left segment of the split BPE as the working electrode, the right segment as the reference electrode, and an external Pt wire, placed in one of the reservoirs, as the counter electrode. Although in this configuration the uncompensated cell resistance is high (Figure S5A) relative to a conventional three-electrode cell (Figure S6), we can still clearly identify Pt oxidation and reduction processes by cyclic voltammetry. Thus, by holding the potential at 1.2 V, we controlled Pt oxide growth and, at −0.6 V, its removal (Figure S5B, black and red traces, respectively). After electrochemically growing Pt oxide on the left segment of the split BPE, we electrically connected both segments and applied E_{tot} of 30 V across the channel. Upon removal of E_{tot}, no fluorescence quenching was observed on the left pole (Figure 4A). In contrast, after electrochemically removing the oxide and connecting both ends of the split BPE, we observed FL fluorescence quenching after briefly applying and then removing E_{tot}. These experiments confirm that the presence of FL fluorescence quenching localized only at the left pole (and not everywhere on the BPE like our simulations suggest) can be explained by the growth of Pt oxide on the right pole while E_{tot} is ON.

Second, we compared the transient fluorescence intensity response of the system in the presence and absence of ferrocenemethanol (FcMeOH), an electrochemically reversible redox reporter that undergoes a one-electron oxidation at potentials lower than water ($E^{o\prime}$ = 0.4 V vs NHE)[45,46] producing neither H^+ nor O_2. We did this by applying E_{tot} of four magnitudes in independent experiments such that ΔE_{elec} (i.e., the magnitude of the combined pole overpotentials) ranged from lower to higher than the activation potential (i.e., the potential required to drive simultaneous oxidation and reduction reactions) of the BPE. We then removed E_{tot} while continuously monitoring FL fluorescence intensity in real time. In the absence of FcMeOH, we did not observe FL quenching at the left pole of the BPE until after the removal of an applied E_{tot} = 40 V or higher (Figure 4B, left column—yellow arrows); that is, a minimum of E_{tot} = 40 V is required to observe quenching of FL at the left pole when water oxidation is the only reaction that can occur. In the presence of FcMeOH, the removal of any applied E_{tot} below 40 V, which provide enough ΔE_{elec} to drive the oxidation of FcMeOH, did not produce fluorescence quenching. Thus, even in the presence of the more easily oxidized FcMeOH, we only observe quenching at the left pole after removing a E_{tot} high enough to drive the water oxidation reaction (Figure 4B, right column—yellow arrows).

Third, we replaced FL with dianionic bodipy disulfonate (BDP), a fluorophore with opposite pH-dependent quenching of fluorescence relative to FL (Figure S3B). BDP also has the added benefit of being insensitive to O_2-induced fluorescence quenching.[47,48] In these experiments, we observed that BDP behaved similarly to FL while E_{tot} was ON (Figure 5, t_1), with

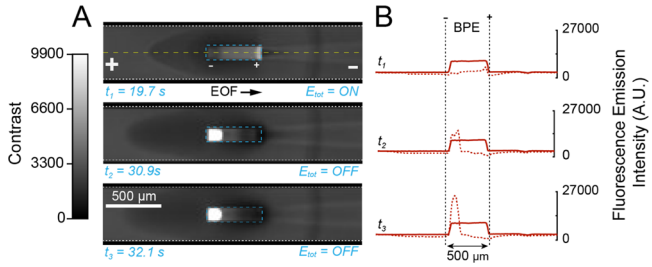

Figure 5. BPE dynamics in the presence of BDP. (A) Fluorescence response of 100 μM BDP in 1.0 mM phosphate (pH 7.5) during (t_1) and after (t_2 and t_3) the application of E_{tot} = 250 V for 30 s in a 600 nm tall channel. Similar to FL, BDP is attracted to and repelled from the right and left BPE poles, respectively, while E_{tot} is ON. Contrary to FL, however, BDP is quenched at high pH; thus, upon removal of E_{tot}, no quenching is observed, following the local fluorescence enhancement at the left pole. Instead, quenching takes place at the right pole. This confirms the pH increase and decrease at the right and left poles, respectively. (B) Quantification of fluorescence emission intensity along the length of the channel (yellow dashed line at t_1 in A). For reference, we added the flat field fluorescent intensity (solid red trace) on all profiles. The complete set of frames can be seen in Movie S2.

the only exception being that a wake of slightly enhanced fluorescence is observed upstream of the right pole. We determined that the underlying cause of such exception was the electrochemical H^+ production/OH^- consumption at the right pole, which lowers the pH, slightly enhancing the fluorescence intensity of BDP (Figure S3B). As was observed with FL, removing E_{tot} produced a localized increase in fluorescence at the left pole (Figure 5, t_2), further validating our simulation's prediction that anions migrate toward this pole (Figure 3C). We therefore concluded that the fluorescence enhancement observed at t_2 for both FL and BDP is not a pH-sensitive phenomenon. Meanwhile, removal of E_{tot} was accompanied by a decrease in BDP fluorescence at the right pole, in agreement with the increased pH also predicted by our simulations (Figure 3D). Finally, after the first localized BDP fluorescence enhancement occurred at the left pole, we observed a second wave of enhancement (Figure 5, t_3) at precisely the same time that FL quenching was

DOI: 10.1021/acsami.9b01339
ACS Appl. Mater. Interfaces 2019, 11, 13777−13786

registered at t_3 in Figure 2, further corroborating that pH acidification occurs at that pole due to water oxidation (Figure S4B) during the BPE's Galvanic discharge.

Collectively, the results shown thus far demonstrate that the sudden drop in FL fluorescence intensity at the left pole (Figure 2, t_3) is indeed caused by water oxidation-driven changes in pH and, possibly, increasing O_2 concentrations during BPE discharge, an event that is independent of self-quenching (Figure S7A) and concentration-dependent photobleaching (Figure S7B).

Quantitative Analysis of Fluorescence Intensity at the Left Pole. In addition to explaining the fundamental physics behind the transient electric and ionic phenomena described above, we exploited the benefits of our device configuration (Figure 1A) to study the relationship between the magnitude of the external electric field and the evolution of the transient effects. Because each of our chips contains nanochannels of different effective lengths (channel 1&5 < channel 2&4 < channel 3), electric fields of different magnitudes are present at any given E_{tot} (Figure S8A). For accurate quantitation, we normalized the maximum ($I_{N,max}$) and minimum ($I_{N,min}$) fluorescence intensities to the flat field using a slightly modified version of the equation by Santiago and co-workers[49]

$$I_N = \frac{(I_m - I_b)}{(I_{ff} - I_b)} \tag{6}$$

where I_N, I_b, I_m, and I_{ff} are the normalized, background, maximum/minimum, and flat field fluorescence, respectively.

By tracking $I_{N,max}$ and $I_{N,min}$ on the left pole at any given time after removal of E_{tot}, we observed that $I_{N,max}$ appears to scale proportionally with the magnitude of the electric field (i.e., channel 1&5 < channel 2&4 < channel 3) because higher electric fields result in more strongly polarized BPEs and thus more intense transient effects (Figure S8B). In contrast, $I_{N,min}$ did not follow the same trend (Figure S8C). We believe this is the case because the fluorescence is close to 100% quenched in all channels and slight differences in electric field strength are harder to detect, making any apparent trend misleading (more experimental evidence supporting these preliminary conclusions is provided by Figure 6A,B and the corresponding discussion in the next paragraph). Because the difference of electric field magnitudes between channels can be approximated numerically, we applied correction factors (see section "Implementation of Correction Factors" and Table S5 of the Supporting Information for details) to channels 1, 2, 4, and 5 relative to channel 3, so that $I_{N,max}$ and $I_{N,min}$ could be compared between all channels. By doing this, we discovered that $I_{N,max}$ for FL and BDP is 1.5 ± 0.1 and 2.19 ± 0.09 (average of three different chips) times higher, respectively, than the flat field. Although much lower than the preconcentration factors achieved by methods designed specifically for ion focusing, such as ion concentration polarization[19] and field-amplified sample stacking,[50] these increased and localized fluorescence values constitute, to the best of our knowledge, the first experimental evidence of ion preconcentration in the absence of an applied potential. Moreover, our method can achieve high FL fluorescence quenching efficiency (91 ± 21% at 250 V) and spatial resolution of $I_{N,max}$ and $I_{N,min}$ events, that is, 91.5 and 100% of all fluorescence enhancement and quenching phenomena,

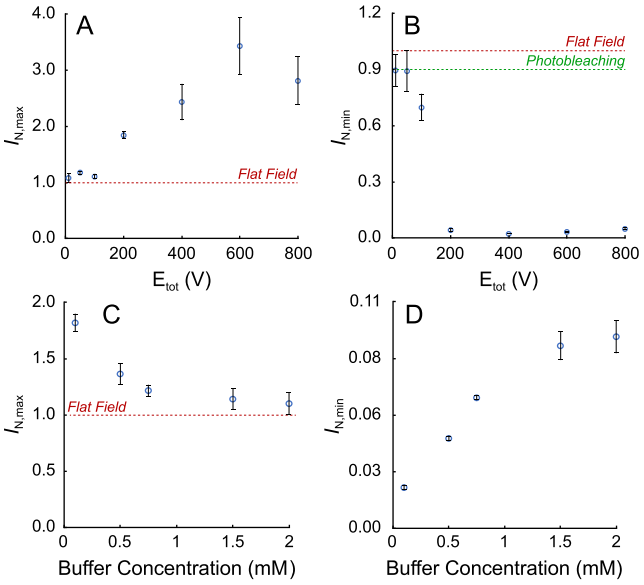

Figure 6. Potential- and electrolyte concentration-dependent fluorescence effects. We normalized the maximum (A,C) and minimum (B,D) fluorescence emission intensities observed in a 600 nm channel containing 100 μM fluorescein in 1 mM phosphate buffer (pH = 7.4 and 8.7, respectively) to the flat field corresponding to each experiment. We demonstrate that the electrokinetic effects originating upon removal of E_{tot} induce (A) enrichment and (B) quenching of the observed FL fluorescence in a manner that is E_{tot}-dependent (held for 30 s). This indicates that a larger applied E_{tot} induces more BPE polarization and, thus, stronger charge imbalances and BPE discharge. In addition, varying the buffer concentration also affects the resulting fluorescence emission intensity once E_{tot} is removed. We demonstrate that the extent of (C) fluorescence enrichment and (D) quenching of FL fluorescence increases with decreasing buffer concentration. Red dashed lines represent the flat field fluorescence. Green dashed line shows the level of photobleaching plus accumulated electrophoretic depletion achieved at the culmination of each video (i.e., frame 500 in Figure S2). Error bars correspond to the standard deviation of average measurements performed on five different channels.

respectively, observed after the removal of E_{tot} took place within 125 μm of the left BPE edge (Figure S9).

Motivated by these results, we investigated the dynamic range of E_{tot} values that drive the transient effects. In doing so, we observed that larger electric field magnitudes (i.e., bigger E_{tot}) results in larger BPE polarization and more efficient fluorescence enhancement, $I_{N,max}$, and quenching, $I_{N,min}$, events (Figure 6A,B, respectively). At E_{tot} values larger than 600 V, however, the electrolysis of water produced bubbles that optically and electrically obstructed the channels, causing a decrease in $I_{N,max}$ (Figure 6A).

The charge imbalances generated when E_{tot} is removed are short-lived and dissipate quickly via (a) migration of ions and (b) charge transfer via water oxidation, inducing transient fluorescence enhancement and quenching effects. Over time, the most significant event that causes dissipation of these charge imbalances is the transport of $H_2PO_4^-$, HPO_4^{2-}, and Na^+ (Figure 3C,D). Thus, by varying the concentration of the background electrolyte, and consequently the concentration of these ions, we observed that the magnitudes of $I_{N,max}$ and $I_{N,min}$ increases 2-fold and decreases by 5-fold, respectively, with decreasing buffer concentration (Figure 6C,D). $I_{N,max}$ increases because, with lower $H_2PO_4^-$ and HPO_4^{2-} concentrations, a higher concentration of FL anions is needed to neutralize the

DOI: 10.1021/acsami.9b01339
ACS Appl. Mater. Interfaces 2019, 11, 13777−13786

positive EDL near the left pole. $I_{N,min}$ decreases because lower concentrations of $H_2PO_4^-$ and HPO_4^{2-} ions locally decrease the buffering capacity of the electrolyte, causing a more drastic drop in pH (also supporting the notion that FL quenching at the left pole is pH-induced). We discount any contributions of the EDL thickness to the magnitudes of $I_{N,max}$ and $I_{N,min}$ because both normalized intensities are largely unaffected by the height of the channel (Figure S10).

We should note that the transient fluorescence enhancement and quenching events cannot be observed in microchannels (Movie S3) for two major reasons. First, flow in microchannels can be affected by pressure. When E_{tot} is ON, EOF drives fluid into the right reservoir (Figure 1A), increasing its total volume with respect to the left reservoir. Thus, when E_{tot} is removed, gravity-induced pressure-driven flow is immediately initiated toward the left reservoir, hindering the expected transient dynamics. Second, the number of FL and BDP ions present in the channel's cross section probed by the optics is much larger for taller channels, thus small changes in fluorescence intensity within the nanoscale EDL regions are more difficult to detect.

CONCLUSIONS

The combined use of nanoconfined bipolar electrochemistry and fluorescence detection allowed us to observe and thoroughly study the rich, coupled electrokinetic and electrochemical phenomena occurring immediately following the removal of an externally applied electric field. Through experimentation and with the aid of finite-element numerical simulations, we demonstrate that short-lived and fluorophore-dependent fluorescence enhancement and quenching events are generated due to nonequilibrium charge imbalances and BPE discharge by water oxidation. Importantly, the extent of such fluorescence events can be quantified and controlled by simply varying the rate of water electrolysis (i.e., by varying the magnitude of the externally applied electric field via the applied E_{tot}), the concentration of the background electrolyte, the type of fluorophore used, and the growth of oxide on the BPE surface.

The transient events described in this manuscript are directly related to the rate of water electrolysis at the BPE and could be exploited for interesting analytical applications. For example, we have preliminary results showing that the fluorescence enhancement observed at the left BPE pole upon removal of E_{tot} is 10-fold higher for a BPE made of Pt versus Au when water electrolysis is the only reaction that can occur. We strongly believe that with careful, thorough experimentation, we and others could use the phenomena described here (together with precisely selected inner-sphere reactions) to screen for electrocatalysts in a parallel and optical manner.

EXPERIMENTAL SECTION

Chemicals and Materials. All solutions were prepared with deionized water (<18.0 MΩ cm, Milli-Q Gradient System, Millipore, Bedford, MA) and filtered through 0.2 μm Nalgene Syringe filters (Thermo Fisher Scientific, Pittsburg, PA) before use. Sodium phosphate monobasic monohydrate was obtained from EMD (Burlington, Massachusetts). Sodium phosphate dibasic heptahydrate, sodium hydroxide, and sodium chloride were purchased from Thermo Fisher Scientific (Pittsburg, PA). Sodium fluorescein salt was purchased from Riedel-de Haën. BODIPY 492/515 disulfonate (4,4-difluoro-1,3,5,7,8-pentamethyl-4-bora-3*a*,4*a*-diaza-*s*-indacene-2,6-disulfonic acid, disodium salt) was acquired from Life Technologies Corporation (Carlsbad, CA). Ferrocenemethanol (97%), acetone, isopropyl alcohol (IPA), sulfuric acid (H_2SO_4), hydrogen peroxide (H_2O_2), *N*-methyl-2-pyrrolidone (NMP), and hexamethyldisiloxane (HMDS) were obtained from Sigma-Aldrich (St. Louis, MO). Luer lock tube fittings were acquired from McMaster-Carr (Santa Fe Springs, CA). Quartz wafers (4″, 525 μm one-side polished, Id: 4W55-325-15C) were obtained from Hoya Corporation (Milpitas, CA). Platinum wires were purchased from Omega Engineering, Inc. (Stamford, CT). CW2400 silver epoxy was acquired from Circuit Works (Chemtronics, Kennesaw, Georgia). Super glue was obtained from Loctite (Loctite, Westlake, Ohio). AZ4110, AZ nLOF 2020, and SU8-2000.5 photoresists; AZ400K (4:1 ratio), AZ 300 MIF, and SU8 developers; and AZ EBR edge bead remover were obtained from MicroChem (Westborough, MA).

Preparation of Working Solutions. Weakly buffered solutions of the different dyes were prepared by adding the appropriate mass of sodium fluorescein salt, BDP, and ferrocenemethanol. The weak buffer was prepared by adding the correct ratio of sodium phosphate monobasic monohydrate and sodium phosphate dibasic heptahydrate to reach the desired concentration, pH [using Ross Ultra Semi-Micro pH electrode (Orion, Thermo Fisher Scientific, Pittsburg, PA) attached to Orion Star A214 pH-meter (Thermo Fisher Scientific, Pittsburg, PA)] and conductivity [with small additions of NaCl, Oakton Benchtop CON 2700 Meter (Cole-Parmer, Vernon Hills, IL)]. All solutions were kept away from light by covering the vials with aluminum foil when not in use.

Nanofluidic Device Fabrication. The device fabrication protocol is summarized in Figure S11. Briefly, two quartz wafers were cleaned, in order, in acetone and IPA for 3 min by sonication. Any remaining organic solvent was removed by thorough rinsing in DI water. One of the wafers was dried at 135 °C for 5 min to remove any moisture from its surface. At this point, HMDS was vapor-deposited on the wafer for 5 min, making the surface hydrophobic to enhance photoresist adsorption. Next, photoresist AZ4110 was spin-coated at 4000 rpm for 30 s, soft baked at 95 °C for 1 min, and exposed to UV light using an MJB 3 UV400 mask aligner from Karl Suss America (Garching, Germany) in the presence of a chrome mask containing the channel's design. The exposed photoresist was removed by immersing the wafer in the AZ400K developer for 1 min and thoroughly rinsed with DI water. The wafer was hard-baked at 120 °C for 3 min, plasma-cleaned, and etched to the desired channel height using a Panasonic E640 etcher from Panasonic Factory Solutions (Rolling Meadows, IL). The remaining photoresist was removed by sonication in acetone and then in IPA for 3 min, rinsed well with water, and dried. The channel depth was measured with a Dektak 6M surface profilometer from Veeco Metrology LLC (Plainview, NY). A second layer of HMDS and AZ4110 photoresist was applied in the same manner as explained above before aligning a second mask—containing the electrode features—and exposing to UV light. The exposed areas were removed by developing in AZ400K for 1 min and rinsing well with DI water. After drying at 120 °C for 3 min, the wafer was plasma-cleaned before 20 nm of Ti, and 80 nm of Pt was deposited (in that order) via a load-locked metal evaporator dual gun from Temescal (Livermore, CA). Lift-off of the metals was performed by immersing the wafer in acetone and sonicating for 20 min. Immediately after the wafer was transferred to IPA, it was sonicated for 3 min, thoroughly rinsed with DI water, and dried. The height (100 nm) of the total metal deposited inside the channels was measured with the profilometer.

Holes (i.e., reservoirs) were drilled on the second wafer using a Sherline/Flashcut model 2000 CNC mill (Vista, CA) before sonicating in acetone and IPA for 3 min each, and thoroughly rinsing with DI water. Here, both wafers were then cleaned in 50:1 H_2SO_4/H_2O_2 at 50 °C for 15 min, rinsed with water for 10 min, and dried at 135 °C for 5 min. The wafers were subjected to 20 s of nitrogen and oxygen plasma using an EVG810LT Low Temp plasma activation system from EVG Group (Albany, NY), aligned and hand-pressed for bonding. Finally, the devices were diced from the bonded wafers using an ADT dicing saw from Advanced Dicing Technologies Ltd. (Yokneam, Israel). Figure 1A shows the dimensions of the final nanofluidic device.

DOI: 10.1021/acsami.9b01339
ACS Appl. Mater. Interfaces 2019, 11, 13777−13786

Microfluidic Device Fabrication. The BPEs were patterned on a quartz wafer using the same protocol mentioned above, with the exception that no dry etching was performed prior to metal deposition. Instead, the channels were fabricated by pouring two-part PDMS on a silicon mold containing 10 μm tall features. After curing the PDMS at 65 °C for 2 h, the desired PDMS part was cut out using a razor blade and reservoirs were created using a 2 mm diameter hole puncher. Dicing of the quartz wafer was performed in the same manner as mentioned in the previous section. Next, both the PDMS containing the microchannels and the quartz wafer containing the BPEs were cleaned with acetone and water before placing in a UV/ozone probe and surface decontamination unit from Novascan Technologies (Milwaukee, WI) for 9 min. After ozone treatment, the device was assembled by aligning and pressing the PDMS onto the quartz piece and baking at 65 °C for 5 min. Immediately after, water was placed in one of the reservoirs for wet storage until use.

Split BPE Device Fabrication. Two quartz wafers were cleaned in piranha solution at 80 °C for 20 min, rinsed with DI water, and blow-dried with N_2. Next, one of the wafers was dehydrated on a 110 °C hotplate for 5 min before spin-coating HMDS and AZ nLOF 2020 photoresist (MicroChem) and soft baking, sequentially, at 115 °C for 120 s and 110 °C for 60 s. At this point, a mask with the split BPE design was aligned with the wafer and both were exposed to UV light, followed immediately by a 60 s bake at 110 °C. The negative photoresist was developed in AZ 300 MIF for 60 s, rinsed in DI water, and dried with N_2. The photoresist pattern was then inspected optically to ensure total development of the photoresist and proper pattern transfer from the mask to the wafer. Next, 20 nm/80 nm Ti/Pt was deposited on the whole wafer via the load-locked metal evaporator dual gun from Temescal. Metal patterning was achieved by lift-off of the photoresist in NMP at 80 °C for 30 min with mild agitation in a heated sonicator. The wafer was sequentially rinsed in acetone, IPA, and DI water before drying with N_2 and dehydrated on a hotplate at 110 °C for 5 min. To define the channel geometry, SU8-2000.5 was then spun on at 3000 rpm with a spin rate of 300 rpm/s followed by edge bead removal at 500 rpm using a swab soaked in AZ EBR Edge Bead Remover. At this point, the wafer was soft baked at 95 °C for 1 min before aligning a second mask (containing the channel geometry) and exposing to UV light. This was immediately followed by a post exposure bake at 95 °C for 1 min before developing in the SU8 developer for 1 min. The wafer was then rinsed with DI water and dried with N_2.

Holes (i.e., reservoirs) were drilled through the second wafer using a Sherline/Flashcut model 2000 CNC mill (Vista, CA) before sonicating in acetone and IPA for 3 min each, and thoroughly rinsing with DI water. Both wafers were then piranha-cleaned at 80 °C and thoroughly rinsed with DI water. To bond the wafers, they were subjected to 20 s of nitrogen and oxygen plasma using an EVG810LT Low Temp plasma activation system before aligning and hand-pressing them together. The semibonded wafer stack was then placed into SUSS SB6-8E Wafer Bonder from Karl Suss America (Garching, Germany), where the wafers were automatically pushed together with 300N of force at 175 °C for 15 min. The bonded wafers were then allowed to cool slowly before the individual devices were diced from the bonded wafers using an ADT dicing saw.

Chip Holder Fabrication. The chip holder was designed with a student design kit from SolidWorks 2017 SP 4.1 (Waltham, MA) and printed with the Object30 Pro 3D printer (Stratasys, Prairie, MN) using veroblackplus RGD875 material. The reservoirs were designed to contain threads compatible with luer lock fittings for applied vacuum.

Device Treatment before Experimentation. All the devices were stored away from air flow and dust particulates until used. Once assembled into the chip holder, 10 μL of 0.1 M NaOH was placed in one of the reservoirs, while vacuum was applied to the other for 15 min to fill the channel and homogenize the wall charges. Next, DI water was used to thoroughly rinse the reservoir where NaOH was added and flowed through the channel for 5 min by vacuum (this was carried out twice) to remove any remaining NaOH. Finally, the solution of interest was introduced to the channel by vacuum flow for 5 min. The polarization of the driving electrodes was such that the direction of EOF was the same as the direction of vacuum flow. The polarization of the driving electrodes, as well as the direction of vacuum-induced flow, was flipped between experiments to prevent Pt from oxidizing only on one side of the BPE. This assured good reproducibility (≤10% RSD) between repetitions of the same experiment.

Fluorescence Experiments. After the water rinse mentioned in the previous section, a background fluorescence image was acquired with an Olympus IX73 inverted microscope (Olympus, Center Valley, PA) coupled to an Andor Technology iXon Ultra EMCCD (Oxford Instruments, Concord, MA) camera and used for background subtraction of all the frames within the same experiment. Once the solution of interest was introduced to the channel, the vacuum setup was removed from the reservoir, and the reservoir was cleaned and filled with the solution of interest. At this point, one Pt wire was introduced to each reservoir, the chip holder (containing the device and the Pt electrodes) was placed onto the fluorescence microscope, and the Pt wires were connected to a Keithley 2410 voltage source (Keithley Instruments, Inc., Cleveland, OH). Data acquisition was set up using Andor iXon Ultra 897 software (Oxford Instruments, Abingdon, UK) with an acquisition time of 2 s at 3.2995 Hz during 500 frames (unless otherwise indicated), for a total of 2.53 min. At time 0 s, data acquisition was initiated. After 10 s (~frame 33), the desired E_{tot} was applied for 30 s and then removed (~frame 132).

Data Analysis of Fluorescence Experiments. All fluorescence images and videos were background subtracted, and all plot profiles were obtained using ImageJ V2 1.52e. A Python v3.6.3 code (provided in the Supporting Information section) was created to quantitatively extract information regarding the magnitude, time, and placement on the BPE of the fluorescence maxima and minima.

Electrochemical Experiments. All electrochemical experiments were performed using a CHI 1242B handheld potentiostat from CH Instruments, Inc. (Austin, TX). When using a typical three-electrode cell, a 10 μm in diameter Pt working ultramicroelectrode, a Ag/AgCl reference electrode, and a Pt wire counter electrode were used. All cyclic voltammograms and linear sweeps were performed at 1 V/s. In experiments performed with split BPE devices, the scan rate was 20 mV/s for all cyclic voltammograms and linear sweeps.

■ ASSOCIATED CONTENT

Supporting Information

The Supporting Information is available free of charge on the ACS Publications website at DOI: 10.1021/acsami.9b01339.

Numerical simulation 2D image of the EDL formation upon activation of the BPE, extent of photobleaching, fluorescence versus pH titration curve for fluorescein and bodipy dyes, table describing all experimental conditions and chemical species involved, tables showing side-by-side comparisons between experimental and simulated physical phenomena as well as transverse and longitudinal transport time-dependent processes, simulated rate of FL fluorescence enhancement and O_2 and H^+ concentration profiles upon removal of E_{tot}, electrochemical response of split Pt BPEs, electrochemical response of a typical three-electrode cell, controls showing the quenching effect at the left pole is not due to either self-quenching or concentration-dependent photobleaching, numerical and experimental results showing that the maximum and minimum fluorescence intensities achieved upon removal of E_{tot} vary depending on the strength of the external electric field applied, description of correction factor calculations, placement and frequency of fluorescence maxima and minima on the BPEs, fluorescence maxima and minima as a function of channel height, a schematic

DOI: 10.1021/acsami.9b01339
ACS Appl. Mater. Interfaces 2019, 11, 13777−13786

representation of the nanofluidic device fabrication protocol, finite element numerical model and governing equations, and Python code for BPE data analysis (PDF)

Movie S1(AVI)

Movie S2 (AVI)

Movie S3 (AVI)

AUTHOR INFORMATION

Corresponding Author

*E-mail: sumita@engineering.ucsb.edu. Phone: (805) 893-5510.

ORCID

Karen Scida: 0000-0003-2735-0441

Netzahualcóyotl Arroyo-Currás: 0000-0002-2740-6276

Carl D. Meinhart: 0000-0003-0701-2728

Sumita Pennathur: 0000-0003-2227-4005

Author Contributions

K.S., N.A.-C., S.P., and J.C.T.E. designed research. K.S. performed all experiments. A.E. performed all numerical simulations. N.A.-C. wrote Python scripts used for data analysis, helped with the design and interpretation of electrochemical measurements, and provided guidance with the electrochemistry theory employed in numerical simulations. J.C.T.E. and C.M. consulted on numerical simulations and data interpretation. K.S. and S.M. fabricated the devices. K.S. and Y.S. designed the chip holder and Y.S. fabricated it. K.S., N.A.-C., A.E., J.C.T.E., and S.P. wrote the manuscript.

Notes

The authors declare no competing financial interest.

ACKNOWLEDGMENTS

The authors would like to thank Dr. L. Garner for helpful discussions regarding the fluorophores, Dr. B. N. Queenan for valuable contributions to the manuscript, and acknowledge the use of the Microfluidics Laboratory within the California NanoSystems Institute, supported by the University of California Santa Barbara and the University of California, Office of the President. Some of the work was performed at the UCSB Nanofabrication Facility. K.S. was supported by the Otis Williams Postdoctoral Fellowship from the Santa Barbara Foundation.

ADDITIONAL NOTE

[a]When the electric field is OFF, the whole BPE becomes an anode. Because such a nomenclature is confusing, we address each pole as left or right throughout.

REFERENCES

(1) Rica, R. A.; Bazant, M. Z. Electrodiffusiophoresis: Particle Motion in Electrolytes under Direct Current. *Phys. Fluids* **2010**, *22*, 112109.

(2) Bishop, K. J. M.; Drews, A. M.; Cartier, C. A.; Pandey, S.; Dou, Y. Contact Charge Electrophoresis: Fundamentals and Microfluidic Applications. *Langmuir* **2018**, *34*, 6315−6327.

(3) Verleysen, K.; Sandra, P. Separation of Chiral Compounds by Capillary Electrophoresis. *Electrophoresis* **1998**, *19*, 2798−2833.

(4) Gascoyne, P.; Shim, S. Isolation of Circulating Tumor Cells by Dielectrophoresis. *Cancers* **2014**, *6*, 545−579.

(5) Kim, S.-O.; Moon, S.-H.; Kim, K.-W. Removal of Heavy Metals from Soils Using Enhanced Electrokinetic Soil Processing. *Water, Air, Soil Pollut.* **2001**, *125*, 259−272.

(6) Duval, J. F. L.; Minor, M.; Cecilia, J.; van Leeuwen, H. P. Coupling of Lateral Electric Field and Transversal Faradaic Processes at the Conductor/Electrolyte Solution Interface. *J. Phys. Chem. B* **2003**, *107*, 4143−4155.

(7) Leinweber, F. C.; Eijkel, J. C. T.; Bomer, J. G.; van den Berg, A. Continuous Flow Microfluidic Demixing of Electrolytes by Induced Charge Electrokinetics in Structured Electrode Arrays. *Anal. Chem.* **2006**, *78*, 1425−1434.

(8) Park, S.; Yossifon, G. Induced-Charge Electrokinetics, Bipolar Current, and Concentration Polarization in a Microchannel-Nafion-Membrane System. *Phys. Rev. E* **2016**, *93*, 062614.

(9) Duval, J. F. L.; van Leeuwen, H. P.; Cecilia, J.; Galceran, J. Rigorous Analysis of Reversible Faradaic Depolarization Processes in the Electrokinetics of the Metal/Electrolyte Solution Interface. *J. Phys. Chem. B* **2003**, *107*, 6782−6800.

(10) Duval, J. F. L.; Buffle, J.; van Leeuwen, H. P. Quasi-Reversible Faradaic Depolarization Processes in the Electrokinetics of the Metal/Solution Interface. *J. Phys. Chem. B* **2006**, *110*, 6081−6094.

(11) Fosdick, S. E.; Knust, K. N.; Scida, K.; Crooks, R. M. Bipolar Electrochemistry. *Angew. Chem., Int. Ed.* **2013**, *52*, 10438−10456.

(12) Paxton, W. F.; Kistler, K. C.; Olmeda, C. C.; Sen, A.; St. Angelo, S. K.; Cao, Y.; Mallouk, T. E.; Lammert, P. E.; Crespi, V. H. Catalytic Nanomotors: Autonomous Movement of Striped Nanorods. *J. Am. Chem. Soc.* **2004**, *126*, 13424−13431.

(13) Wang, Y.; Hernandez, R. M.; Bartlett, D. J.; Bingham, J. M.; Kline, T. R.; Sen, A.; Mallouk, T. E. Bipolar Electrochemical Mechanism for the Propulsion of Catalytic Nanomotors in Hydrogen Peroxide Solutions. *Langmuir* **2006**, *22*, 10451−10456.

(14) Fosdick, S. E.; Crooks, R. M. Bipolar Electrodes for Rapid Screening of Electrocatalysts. *J. Am. Chem. Soc.* **2012**, *134*, 863−866.

(15) Lin, X.; Zheng, L.; Gao, G.; Chi, Y.; Chen, G. Electrochemiluminescence Imaging-Based High-Throughput Screening Platform for Electrocatalysts Used in Fuel Cells. *Anal. Chem.* **2012**, *84*, 7700−7707.

(16) Guerrette, J. P.; Percival, S. J.; Zhang, B. Fluorescence Coupling for Direct Imaging of Electrocatalytic Heterogeneity. *J. Am. Chem. Soc.* **2013**, *135*, 855−861.

(17) Chow, K.-F.; Mavré, F.; Crooks, R. M. Wireless Electrochemical DNA Microarray Sensor. *J. Am. Chem. Soc.* **2008**, *130*, 7544−7545.

(18) Bouffier, L.; Kuhn, A. Design of a Wireless Electrochemical Valve. *Nanoscale* **2013**, *5*, 1305−1309.

(19) Anand, R. K.; Sheridan, E.; Knust, K. N.; Crooks, R. M. Bipolar Electrode Focusing: Faradaic Ion Concentration Polarization. *Anal. Chem.* **2011**, *83*, 2351−2358.

(20) Laws, D. R.; Hlushkou, D.; Perdue, R. K.; Tallarek, U.; Crooks, R. M. Bipolar Electrode Focusing: Simultaneous Concentration Enrichment and Separation in a Microfluidic Channel Containing a Bipolar Electrode. *Anal. Chem.* **2009**, *81*, 8923−8929.

(21) Scida, K.; Sheridan, E.; Crooks, R. M. Electrochemically-Gated Delivery of Analyte Bands in Microfluidic Devices Using Bipolar Electrodes. *Lab Chip* **2013**, *13*, 2292−2299.

(22) Gao, R.; Ying, Y.-L.; Hu, Y.-X.; Li, Y.-J.; Long, Y.-T. Wireless Bipolar Nanopore Electrode for Single Small Molecule Detection. *Anal. Chem.* **2017**, *89*, 7382−7387.

(23) Wood, M.; Zhang, B. Bipolar Electrochemical Method for Dynamic *In Situ* Control of Single Metal Nanowire Growth. *ACS Nano* **2015**, *9*, 2454−2464.

(24) Darcy, J. W.; Koronkiewicz, B.; Parada, G. A.; Mayer, J. M. A Continuum of Proton-Coupled Electron Transfer Reactivity. *Acc. Chem. Res.* **2018**, *51*, 2391−2399.

(25) Hammes-Schiffer, S. Proton-Coupled Electron Transfer: Moving Together and Charging Forward. *J. Am. Chem. Soc.* **2015**, *137*, 8860−8871.

(26) Saha, S. Anion-Induced Electron Transfer. *Acc. Chem. Res.* **2018**, *51*, 2225−2236.

(27) Bard, A. J.; Itaya, K.; Malpas, R. E.; Teherani, T. Electrochemical and Photoelectrochemical Studies of Excess Electrons in Liquid Ammonia. *J. Phys. Chem.* **1980**, *84*, 1262−1266.

DOI: 10.1021/acsami.9b01339
ACS Appl. Mater. Interfaces 2019, 11, 13777−13786

(28) Combellas, C.; Kanoufi, F.; Thiébault, A. Solutions of solvated electrons in liquid ammonia. *J. Electroanal. Chem.* **2001**, *499*, 144−151.
(29) Schmickler, W. Electronic Effects in the Electric Double Layer. *Chem. Rev.* **1996**, *96*, 3177−3200.
(30) Kuznetsov, A. M.; Medvedev, I. G.; Ulstrup, J. Electric Double Layer Effect on Observable Characteristics of the Tunnel Current Through a Bridged Electrochemical Contact. *J. Chem. Phys.* **2007**, *127*, 104708.
(31) Bazant, M. Z. Induced-Charge Electrokinetic Phenomena. *Electrokinetics and Electrohydrodynamics in Microsystems; CISM Courses and Lectures*; Springer: Vienna, 2011; Vol. *530*, p 75.
(32) Contento, N. M.; Branagan, S. P.; Bohn, P. W. Electrolysis in Nanochannels for in Situ Reagent Generation in Confined Geometries. *Lab Chip* **2011**, *11*, 3634−3641.
(33) Mavré, F.; Anand, R. K.; Laws, D. R.; Chow, K.-F.; Chang, B.-Y.; Crooks, J. A.; Crooks, R. M. Bipolar Electrodes: A Useful Tool for Concentration, Separation, and Detection of Analytes in Microelectrochemical Systems. *Anal. Chem.* **2010**, *82*, 8766−8774.
(34) Panchompoo, J.; Aldous, L.; Baker, M.; Wallace, M. I.; Compton, R. G. One-Step Synthesis of Fluorescein Modified Nano-Carbon for Pd(II) Detection via Fluorescence Quenching. *Analyst* **2012**, *137*, 2054−2062.
(35) Gencoglu, A.; Camacho-Alanis, F.; Nguyen, V. T.; Nakano, A.; Ros, A.; Minerick, A. R. Quantification of PH Gradients and Implications in Insulator-Based Dielectrophoresis of Biomolecules. *Electrophoresis* **2011**, *32*, 2436−2447.
(36) Pourbaix, M. *Atlas of Electrochemical Equilibria in Aqueous Solutions*; Pergamon Press: Oxford, New York, 1966.
(37) Arık, M.; Çelebi, N.; Onganer, Y. Fluorescence Quenching of Fluorescein with Molecular Oxygen in Solution. *J. Photochem. Photobiol., A* **2005**, *170*, 105−111.
(38) Song, L.; Hennink, E. J.; Young, I. T.; Tanke, H. J. Photobleaching Kinetics of Fluorescein in Quantitative Fluorescence Microscopy. *Biophys. J.* **1995**, *68*, 2588−2600.
(39) Martin, M. M.; Lindqvist, L. The PH Dependence of Fluorescein Fluorescence. *J. Lumin.* **1975**, *10*, 381−390.
(40) Chen, X.; Pradhan, T.; Wang, F.; Kim, J. S.; Yoon, J. Fluorescent Chemosensors Based on Spiroring-Opening of Xanthenes and Related Derivatives. *Chem. Rev.* **2012**, *112*, 1910−1956.
(41) Sjöback, R.; Nygren, J.; Kubista, M. Absorption and Fluorescence Properties of Fluorescein. *Spectrochim. Acta, Part A* **1995**, *51*, L7−L21.
(42) Eden, A.; Scida, K.; Arroyo-Currás, N.; Eijkel, J. C. T.; Meinhart, C. D.; Pennathur, S. Modeling Faradaic Reactions and Electrokinetic Phenomena at a Nanochannel-Confined Bipolar Electrode. *J. Phys. Chem. C* **2019**, *123*, 5353−5364.
(43) Perdue, R. K.; Laws, D. R.; Hlushkou, D.; Tallarek, U.; Crooks, R. M. Bipolar Electrode Focusing: The Effect of Current and Electric Field on Concentration Enrichment. *Anal. Chem.* **2009**, *81*, 10149−10155.
(44) Anand, R. K.; Sheridan, E.; Hlushkou, D.; Tallarek, U.; Crooks, R. M. Bipolar Electrode Focusing: Tuning the Electric Field Gradient. *Lab Chip* **2011**, *11*, 518−527.
(45) Cannes, C.; Kanoufi, F.; Bard, A. J. Cyclic Voltammetry and Scanning Electrochemical Microscopy of Ferrocenemethanol at Monolayer and Bilayer-Modified Gold Electrodes. *J. Electroanal. Chem.* **2003**, *547*, 83−91.
(46) Zheng, Q.; Huang, X.; Liu, Y.; Fang, X.; Zhang, J.; Shao, H. Electrochemical Quantification of Intermolecular Hydrogen Bonding between Ferrocenemethanol and 3-Mercaptopropanoic Acid on Gold. *J. Phys. Chem. C* **2017**, *121*, 22123−22129.
(47) Hinkeldey, B.; Schmitt, A.; Jung, G. Comparative Photostability Studies of BODIPY and Fluorescein Dyes by Using Fluorescence Correlation Spectroscopy. *ChemPhysChem* **2008**, *9*, 2019−2027.
(48) Zhang, X.-F.; Yang, X. Singlet Oxygen Generation and Triplet Excited-State Spectra of Brominated BODIPY. *J. Phys. Chem. B* **2013**, *117*, 5533−5539.
(49) Jung, B.; Bharadwaj, R.; Santiago, J. G. On-Chip Millionfold Sample Stacking Using Transient Isotachophoresis. *Anal. Chem.* **2006**, *78*, 2319−2327.
(50) Gong, M.; Wehmeyer, K. R.; Limbach, P. A.; Arias, F.; Heineman, W. R. On-Line Sample Preconcentration Using Field-Amplified Stacking Injection in Microchip Capillary Electrophoresis. *Anal. Chem.* **2006**, *78*, 3730−3737.

DOI: 10.1021/acsami.9b01339
ACS Appl. Mater. Interfaces 2019, 11, 13777−13786